Combined x-ray reflectivity and grazing incidence x-ray fluorescence study of Ta/Cr/Pt thin film stacks

Philippe Jonnard, Karine Le Guen, Renaud Delaunay, Yves Ménesguen, Marie-Christine Lépy, Emrick Briand, Didier Schmaus, Ian Vickridge

Combined x-ray reflectivity and grazing incidence x-ray fluorescence study of Ta/Cr/Pt thin film stacks

Philippe Jonnard[1], Karine Le Guen[1], Renaud Delaunay[1], Yves Ménesguen[2], Marie-Christine Lépy[2], Emrick Briand[3], Didier Schmaus[3], Ian Vickridge[3]

(1) Sorbonne Université, Faculté des Sciences et Ingénierie, UMR CNRS, Laboratoire de Chimie Physique - Matière et Rayonnement (LCPMR), 4 Place Jussieu, F-75252 Paris Cedex 05, France

(2) Université Paris-Saclay, CEA, LIST, Laboratoire National Henri Becquerel (LNE-LNHB), F-91120 Palaiseau, France

(3) Sorbonne Université, CNRS, Institut des NanoSciences de Paris, INSP, SAFIR, F-75005 Paris, France

Abstract

The Ta/Cr/Pt three-layer system can be used as a planar x-ray waveguide, that is to say it can guide an x-ray beam inside its chromium layer. This property comes from the difference in density and hence in optical index between the two “heavy” or cladding tantalum and platinum layers and the “light” or guiding chromium layer. The waveguide will be efficient provided the layers are a few nanometers thick and that the interfaces are as sharp as possible. To control the quality of the stack, we combine grazing incidence x-ray fluorescence (GIXRF) and x-ray reflectivity (XRR) measurements on a series of Ta/Cr/Pt samples, whose only difference is the thickness of the Cr layer. The three considered samples have been deposited by magnetron sputtering and their designed structures are: Ta (8 nm) / Cr (5, 10 and 15 nm) / Pt (14 nm) / Si substrate. The combination of XRR and GIXRF tightens constraints on the parameters used to simulate the stack: thickness, roughness, composition and density of the layers and their interlayers. For each sample we used six GIXRF curves obtained from three different characteristic x-ray lines (Ta Lα, Cr Kα and Pt L$\beta_{2,15}$) excited at three different incident photons energies (6.25, 10 and 12 keV) as well as one XRR curve obtained at 6.25 keV. The XRR-GIXRF combined analysis demonstrates that the Ta/Cr/Pt structure is too simplistic and that it is necessary to introduce some interlayers at the top and bottom of the stacks to obtain a reliable agreement between the experimental and simulated GIXRF and XRR curves.

Introduction

X-ray standing wave methods are now well established in the lab and in synchrotron facilities [1]. They can be applied to study periodic structures, such as crystals or multilayers, as well as stacks of thin films. To proceed, the electric field at the origin of secondary processes, x-ray fluorescence (XRF) or x-ray photoemission, is located in specific places within the sample, so that elemental and chemical information about the sample is depth sensitive. This comes down to measuring the XRF intensity as a function of the grazing angle of the incident radiation or of the detection angle of the emitted radiation. In the first case, the technique is called grazing incidence XRF (GIXRF); in the second case it is called grazing exit XRF (GEXRF) or Kossel diffraction [1–3]. Practically, this is done by changing the geometry of the experiment, *i.e.* by rotating the sample while keeping the detector fixed in GIXRF and GEXRF or by rotating the detector while keeping the sample fixed in GEXRF.

The GIXRF and GEXRF techniques are still evolving to adapt to synchrotron or laboratory environments [4] and to opportunities offered by polycapillaries to perform confocal spectroscopy and imaging [5,6]. This allows studying and quantifying various samples, homogenous [7] or stratified [6], presenting depth concentration gradients [8], etc. These works benefit from the advances made in the models developed for the x-ray standing wave technique combined with x-ray photoelectron, Auger and x-ray emission spectroscopies [9–12].

In this framework, we showed the feasibility of applying Kossel diffraction [13] combined with particle induced x-ray emission (PIXE) for the study of planar x-ray waveguides [14]. These devices are made of thin films, a guiding layer generally made of a light material surrounded by two cladding layers made of heavy materials. This work demonstrated the ability of the PIXE-Kossel methodology to characterize the stacks of nano-scale thin films, through the analysis of two waveguide systems: namely Pt/Fe/Pt and Ta/Cr/Pt. However, the analysis of the Ta/Cr/Pt system was not definitive, as the obtained description of the stack, *i.e.* intermixing taking place between the Ta and Cr layers to form a compound that was subsequently partly oxidized, could still be improved [14].

In this work, we continue our study on the Ta/Cr/Pt system in order to get a better description of the actual stack, that is to say to better understand the interlayers present between the different thin films and the silicon substrate. For that purpose, we perform GIXRF and x-ray reflectivity (XRR) measurements on a series of Ta/Cr/Pt samples, whose only difference is the thickness of the Cr layer. XRR is widely used for thin film analysis. The XRR-GIXRF combination [15,16] constrains the parameters used to simulate the stack: thickness, roughness, composition and density of the layers and their interlayers. This represents many free parameters to fit, without being sure that the fitting process leads to a unique solution. This is why combining various results obtained on the same system leads to a more reliable description of the stack. With this in mind, for each sample we used one XRR curve and six GIXRF curves obtained from three different characteristic x-ray lines excited at three different energies of incident photons. In order to constrain the possible solutions, we also compare the numbers of atoms in stack as deduced from the fitted parameters (thicknesses and densities) to those measured by Rutherford backscattering spectrometry (RBS) and nuclear reaction analysis (NRA).

Experimental

Sample preparation

The three-layer samples were deposited at room temperature on Si (100) substrates by DC magnetron sputtering at LCPMR. The power applied on the high-purity sputtering targets was 10 W, the base pressure 10^{-8} mbar and the sputtering gas argon at a working pressure of 5×10^{-2} mbar. The deposition rates of Pt, Cr and Ta were 0.066, 0.024 and 0.035 nm/s, respectively, as measured by a quartz microbalance. Three waveguides were prepared with the same structure: Ta/Cr/Pt/Si substrate. The target thicknesses of Pt and Ta layers were the same for all samples: 14 and 8 nm, respectively. The samples differ by the targeted thickness of the Cr layer, being 5, 10 and 15 nm. The corresponding samples are labelled “5 nm Cr”, “10 nm Cr” and “15 nm Cr”.

XRR and GIXRF measurements

Experiments were performed on the hard x-ray branch of the Métrologie beamline [https://www.synchrotron-soleil.fr/en/beamlines/metrologie] of the SOLEIL synchrotron facility, with the CASTOR goniometer [17], dedicated to combined XRR and GIXRF experiments. A *p*-polarized radiation was used for all the experiments. An AXUV Si photodiode was used for the θ-2θ reflectivity measurement with incident photons of 6.25 keV.

A silicon drift detector (SDD), placed at 90° with respect to the incident beam, acquired the x-ray fluorescence. The geometry and configuration of the experiment (size of the incident beam, size of the sample, distance between sample and SDD, distance and size of the collimator in front of the SDD, etc.) were checked so that the geometrical factor, necessary to compare experiments and simulations [18], can be determined. Three incident photon energies were chosen:

- 6.25 keV, in order to only measure the Cr Kα (2p-1s transition) and Kβ (3p-1s) lines;
- 10 keV, just above the Ta L3 ionization threshold, in order to obtain the Cr K lines and the Ta Lα (3d-$2p_{3/2}$), Lβ_6 (4s-$2p_{3/2}$), L$\beta_{2,15}$ (4d-$2p_{3/2}$) and Ll (3s-$2p_{3/2}$) lines;
- 12 keV, just above the Pt L3 ionization threshold, in order to obtain the Cr K and Ta L lines, and the many Pt L lines coming from the radiative de-excitation of the Pt $2p_{3/2}$ level.

The x-ray spectra were recorded by the SDD for many glancing angles of the incident radiation on the surface of the sample, ranging from 0° (incident beam parallel to the surface) to 3°. The acquisition time for each angle was either 30 or 100 s.

To build the GIXRF curves, that is to say the variation of the intensity of characteristic x-ray lines as a function of the glancing angle of the incident radiation, first the x-ray spectra need to be processed to determine the net area of each characteristic peak. This was done with the COLEGRAM software [19], a user-friendly interface to process x-ray spectra. To analyse several similar spectra with COLEGRAM, the user must create a model on one spectrum and a batch fitting is available to process large number of spectra with the same peaks (number, positions, constraints on parameters), fitting on the remaining free parameters (amplitudes, …). Several peak shapes are available for the user. We chose to use gaussians with condition upon standard deviation: it is an option to account for the variation of the instrumental width with energy. The standard deviation of the peaks becomes $\sigma^2 = \sigma_0^2 + k.E$ where k and σ are the new fitting parameters common to all peaks. A Levenberg-Marquardt algorithm performs the peak fitting.

The spectrum decomposition is a critical step as some line interferences are possible owing to the limited spectral resolution (130-150 eV) of the SDD in this photon energy range. To overcome this problem during the fitting procedure, we put constraints on the positions of most peaks in order to limit misfits. Nevertheless, whereas the most intense lines of the Cr and Ta spectra were used, it was not possible to use the Pt Lα (Lα$_1$ at 9442 eV and Lα$_2$ at 9362 eV [20]) reliably owing to the proximity of the Ta Lβ$_6$ (9315 eV [20]) line. In this case the Pt Lβ$_{2,15}$ line was used, because it can be separated more easily. An example of spectrum decomposition is shown in Figure 1(a). We have validated the spectra fitting procedure by checking that the GIXRF curves obtained from different emissions of the same element have the same shape, differing only by their relative intensities. This is illustrated in Figure 1(b) in the case of tantalum, for which the four considered emissions are normalized to their maximum. It can be seen that even the Ta Lβ$_6$ GIXRF curve could have been used, however with a much lower intensity, as its shape is the same as those of the three other Ta L emissions.

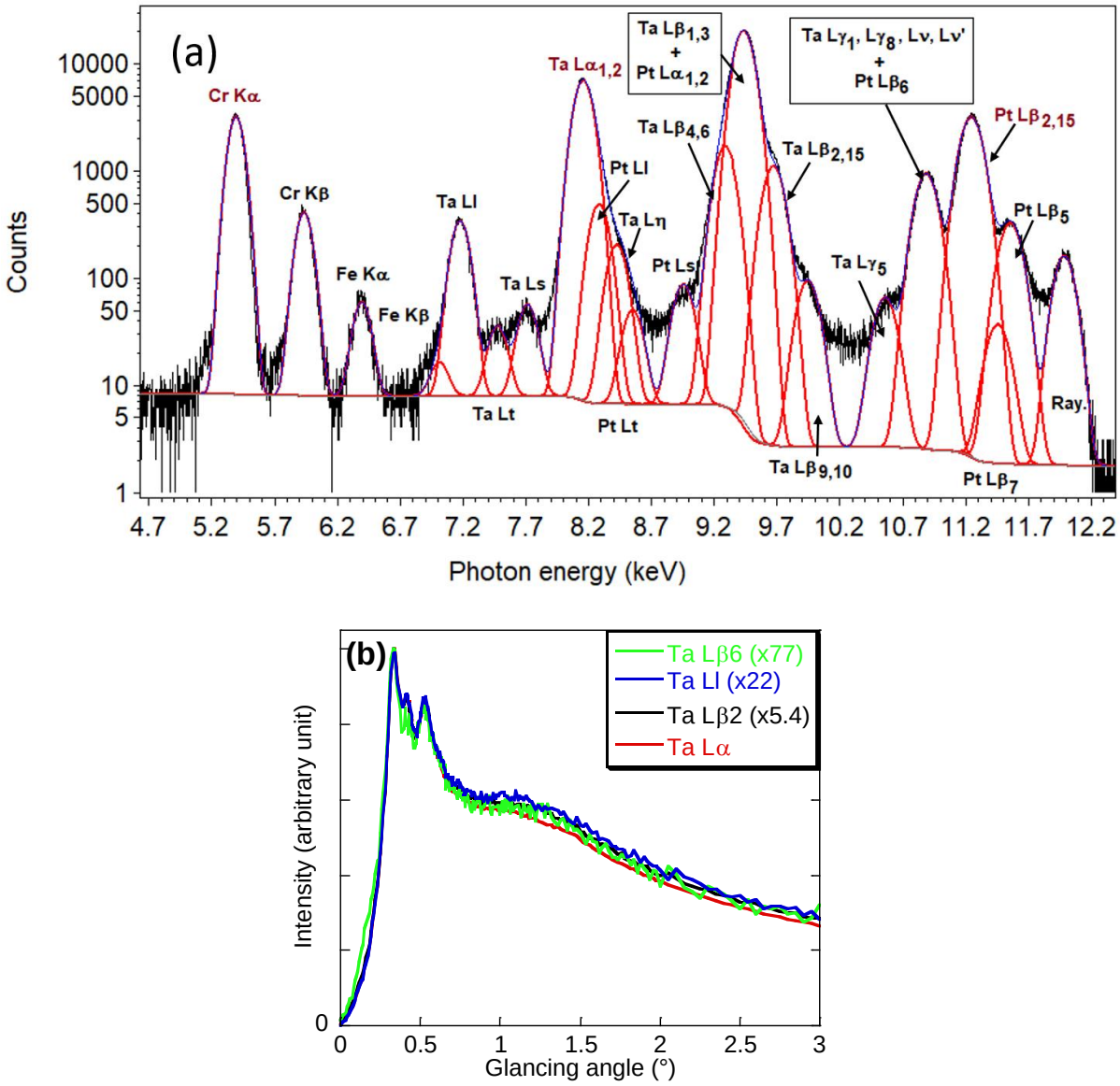

Figure 1: (a) Decomposition of the x-ray spectrum (in log scale) emitted by sample "5 nm Cr" excited at 12 keV under a glancing angle of 0.5° (dots: experiment; red lines: characteristic peaks; pink line:

background); the lines written in brown colour are those used to obtain the GIXRF curves; the peak note "Ray." is due to the scattering of the incident radiation; (b) GIXRF curves obtained with different L emissions of tantalum excited at 12 keV; the number in parenthesis is the multiplying factor to get the same maximum as the one of the Lα emission.

XRR and GIXRF simulations

The x-ray reflectivity was simulated using the Parratt recursive formula [21] together with the Névot-Croce formalism [22] to account for the interface roughness. At glancing angles, the limited sample length produces geometrical effects, which are taken into account. In the optimization procedure we use a cost (or merit) function that emphasizes the very low reflectivity values at high angles, that is to say XRR(θ) × θ^5. Multiplying the reflectivity by a power of the angle gives more importance to the reflectivity at high angles where its absolute value decreases exponentially. Otherwise the values below the critical angles are often dominating the chi2 estimation.

Calculating the emitted fluorescence of a specific element from the sample starts with the evaluation of the x-ray standing wave field inside the structure. The Parratt recursive algorithm used for XRR gives the value of forward and backward electric fields at the centre of each layer [21]. In *p*-polarisation, the calculation of the Parratt recursive formula is made on the magnetic field instead of the electric one. H_t and H_r are the transmitted and reflected magnetic field component of the electro-magnetic field representing the photon respectively. H_t and H_r are dimensionless as the units are carried by the flux of photons. In order to take into account the variation of the field and the interface roughness, our model cuts the layers into thin slabs. The detected fluorescence is derived using the following equation:

$$XRF_i(\theta) = \Omega(\theta) \times I_0 \times T \times \eta_i \times \tau_i \times \omega_i \times \sum_j W_i(z_j) \times \rho(z_j) \times (z_j - z_{j-1}) \times \left\| \frac{H_t(z_j,\theta)}{n_j} + \frac{H_r(z_j,\theta)}{n_j} \right\|^2 \times exp\left(-\sum_{h=1}^{j-1} \mu_i(z_h) \times \rho(z_h) \times (z_h - z_{h-1}) \right)$$

where *T* is the live time of each spectrum, *i.e.* the acquisition time (in *s*) taking into account the detector dead time), I_0 the flux of incident photons (s^{-1}), η_i the detector full absorption peak efficiency at the line energy of element *i*, τ_i the photoelectric cross sections($cm^{-2}.g^{-1}$) of element *i* at the incoming photon energy and ω_i the partial fluorescence yields of element *i* (corresponding to the shell fluorescence yield multiplied by the line contribution to the shell or subshell fluorescence yield). The solid angle $\Omega(\theta)$ must be calculated for each glancing angle θ. The case where the line is excited by several subshells due to the Coster-Kronig cascade is taken into account as well. The parameter $W_i(z_j)$ corresponds to the weight fraction of element *i* at depth z_j (*cm*) and $\rho(z_j)$ (g.cm^{-3})is the density at the same depth and n_j being the optical index.The emitted fluorescence is reabsorbed when passing through the upper slabs and the exponential term accounts for this attenuation. In the fitting procedure, we use a differential method including XRR and GIXRF curves as experimental inputs, with layer densities, thicknesses, roughnesses and elemental weight ratios as fitting parameters. The fitting procedure stops when the χ^2 cannot be further diminished. In this process, secondary fluorescence, for example excitation of the Cr Kα line by Pt L lines, is not considered.

Owing to the large number of parameters necessary to describe the multilayer stacks it is preferable to perform a combined fit of the XRR and GIXRF curves since this is well known to constrain the parameters [15,23,24]. In this process, a global merit function is calculated by considering at the same time the differences between experimental and simulated curves, which in turn is used to determine the variation of the fitted parameters. Moreover, this avoids the cumbersome iterative cycle of first obtaining an XRR fit, then using the deduced parameters as the starting point for the GIXRF fit and then coming back to the XRR fit until the agreement between both fits is satisfactory.”.

RBS and NRA measurements

The Ta, Cr and Pt projected atomic areal densities were determined by RBS, at the SAFIR platform of Sorbonne Université, with $^4He^+$ ions of 2028 keV at normal incidence (0°) or at 40, 65 and 80° from normal. The more the sample is tilted, the more the Ta and Pt emission lines are resolved. We used a reference containing 6.0 x 10^{15} Bi/cm^2 implanted about 20 nm into Si. The backscattered He ions were detected at a scattering angle of 165° with respect to the beam direction, for an incident fluence of 10 µC (6.3 x 10^{13} ions) and beam current of about 70 nA directed into a 1mm beam spot. As an example, we show in Figure 2, the RBS spectrum of the “15 nm Cr” sample. The peaks corresponding to Cr, Ta and Pt are well resolved. The silicon substrate is seen as an edge. Because the scattering cross section is small for oxygen, no oxygen signal is visible above the background. In Table 1 we present the measured areal densities and corresponding thicknesses calculated assuming the densities of the bulk materials, which leads:

- for 1 nm bulk Ta to 5.54 x 10^{15} Ta/cm^2;
- for 1 nm bulk Cr to 8.33 x 10^{15} Cr/cm^2.
- for 1 nm bulk Pt to 6.63 x 10^{15} Pt/cm^2.

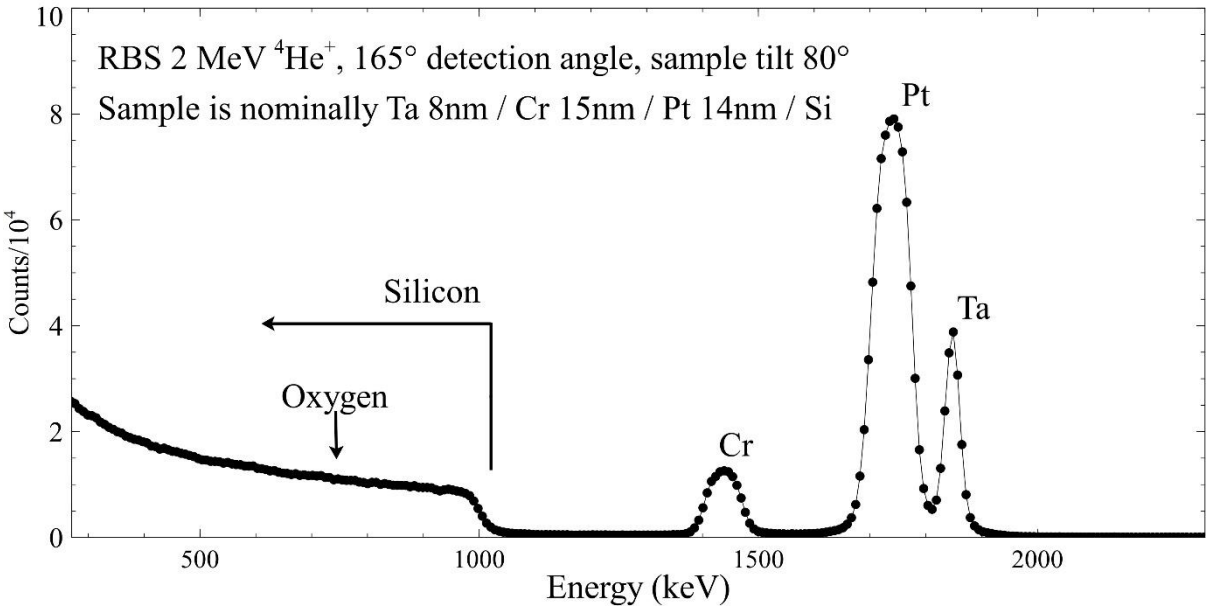

Figure 2: RBS spectrum obtained with the “15 nm Cr” sample.

Because oxygen is not visible in the RBS spectra, the oxygen atomic areal densities were also determined at the SAFIR Platform by NRA with the $O^{16}(d,p)O^{17}$ reaction using 845 keV deuteron ions at normal incidence, which is much more sensitive than RBS here. A deuteron fluence of 100 µC was used, obtained with a beam current of about 160 nA in a 2 mm beam spot. For absolute quantification we used a thin oxide reference containing 700 x 10^{15} O/cm^2. The protons were detected at 90° and the

sample surface was tilted 52° towards the detection angle with respect to the direction of the incident beam. Results are summarised in Table 1. Let us note that the amount of O^{16} on the bare Si sample (without any layer on top) is determined to be 2.15 x 10^{16} O/cm^2.

Table 1: In the three TaCrPt samples, determination of the concentrations and thicknesses of Ta, Cr and Pt as obtained by RBS and of O by NRA. Thicknesses are calculated assuming the densities of the bulk materials as indicated in the first line.

Sample	Ta 16.65 g/cm^3 Ta (Ta/cm^2) Ta (nm)	Cr 7.19 g/cm^3 Cr (Cr/cm^2) Cr (nm)	Pt 21.46 g/cm^3 Pt (Pt/cm^2) Pt (nm)	O (O/cm^2)
"5 nm Cr"	2.1 x 10^{16} 3.8 nm	5.86 x 10^{16} 7.03 nm	10.5 x 10^{16} 15.8 nm	1.78 x 10^{16}
"10 nm Cr"	2.56 x 10^{16} 4.62 nm	11.5 x 10^{16} 13.8 nm	10.1 x 10^{16} 15.2 nm	1.65 x 10^{16}
"15 nm Cr"	2.69 x 10^{16} 4.86 nm	15.7 x 10^{16} 18.8 nm	10.2 x 10^{16} 15.4 nm	1.77 x 10^{16}

The relative uncertainty on the atomic concentrations is estimated to be ±5% for Cr, ±3% for Ta and Pt and ±5% for O. In the case of the "5 nm Cr" sample, the uncertainty in the determination of Ta and Pt is larger, about ±12%, because the Ta and Pt lines are not well resolved in this case. The Ta thickness is almost half of the nominal thickness, 8 nm, owing to some calibration uncertainty of the deposited thicknesses most probably related to the aging of the quartz crystal used to perform the thickness measurement. The number of Cr atoms increases almost linearly with the aimed thickness and is 30-40% higher than expected, probably owing to some calibration uncertainty. Within the experimental uncertainty, as expected the numbers of Ta, Pt and O atoms are constant in the three samples.

Results and discussion

A set of results for a given sample consists in the XRR curve obtained at 6.25 keV, the Cr K GIXRF curve obtained at 6.25 keV, the Cr K and Ta L GIXRF curves obtained at 10 keV and the Cr K, Ta L and Pt L GIXRF curves obtained at 12 keV, *i.e.* a total of 7 curves. As an example, we present in Figure 3 the set of results for the "15 nm Cr" sample. The XRR pattern is characteristic of a stack of thin films, the numerous oscillations coming from the interferences between the beams reflected on the surface, on the substrate and at the interfaces. The GIXRF curves are normalized with respect to their acquisition time in order to be plotted on the same graph. They are also plotted on a transfer wave-vector scale rather than as a function of the glancing angle in order to display all the curves relative to the same element on the same figure. For a given element, the features in the GIXRF curves occur at the same value of the transfer vector for the curves obtained at 6.25 and 10 keV. However, for the Cr and Ta curves obtained at 12 keV, the features are slightly shifted by around +0.04 nm^{-1}. This indicates a small misalignment, probably coming from the difficulty to work at very small glancing angles. The intensity difference between the GIXRF curves of a given element is related to the value of the photoionization cross section, higher when the photon energy is closer to the ionization threshold.

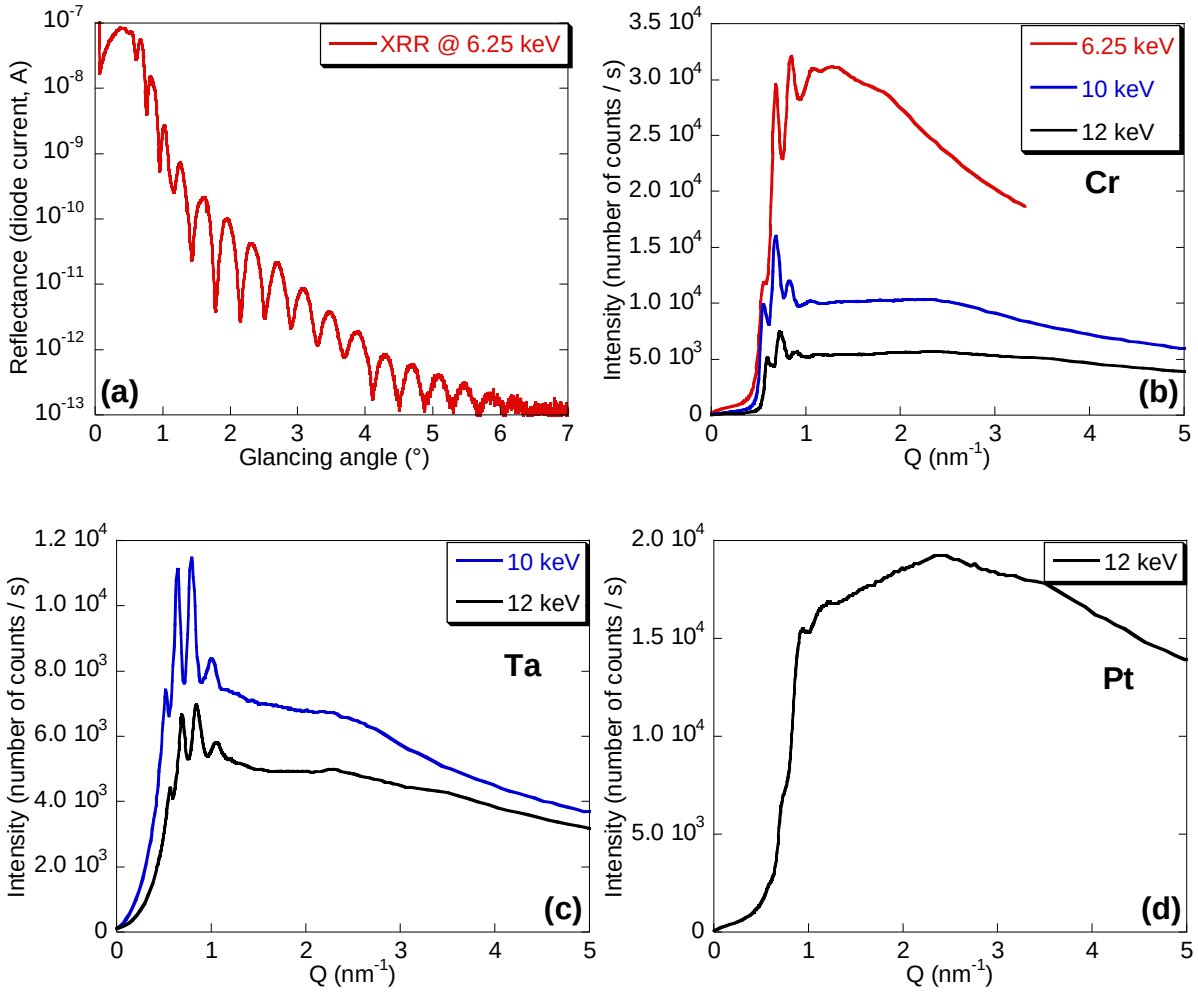

Figure 3: For the "15 nm Cr" sample: (a) reflectivity curve (in log scale); GIXRF curves (in linear scale) of (b) Cr Kα, (c) Ta Lα and (d) Pt L$\beta_{2,15}$.

It appeared that it is not possible to simulate the experimental curves by using a model of the structure consisting only of the three Ta, Cr and Pt layers having the aimed thicknesses. Indeed, some superficial oxidation occurs, the interfaces between the different layers can be reactive and some drift of the deposition rates away from their calibrated values is always possible. For example, the mixing enthalpies, calculated with the Miedema model [25], between the different layers are all negative: Pt-Si, -49 kJ/mol; Cr-Pt, -24 kJ/mol; Cr-Ta, -6.9 kJ/mol, meaning that intermixing is energetically possible at all the interfaces.

The strategy to fit the set of results is to use as simple a model of the stack as possible. If it is not possible to obtain a good fit, then an interlayer is added in the description of the stack. Starting from the designed Ta/Cr/Pt/Si substrate system, first the oxidation of the top Ta layer is added. The stoichiometric compound Ta_2O_5 is considered. Then, an interlayer is added either at the Ta-on-Cr, Cr-on-Pt or Pt-on-Si interface. The structure with the last interlayer gives a satisfying fit, so we do not consider addition of a second interlayer. Let us note from the mixing enthalpies that intermixing is expected to be the easiest at the Pt-on-Si interface. The composition of the interlayer was also one of the fitted parameters. This process was followed for the "Cr 10 nm" sample. Then, the two other samples were fitted with the same structure (thickness, roughness, density and composition of the layers) as that of "Cr 10 nm" as a starting parameter. Only the Cr layer thickness was changed according

to the expected thickness of the sample. For “Cr 5 nm” and “Cr 15 nm” the composition of the interlayer was not searched and fixed at that of “Cr 10 nm”.

An example of the fit of the set of results for the sample “Cr 10 nm” is given in Figure 4(a)-(d). Here we present only the GIXRF curves of Cr obtained at 6.25 keV, of Ta obtained at 10 keV and of Pt obtained at 12 keV, as we have seen in Figure 3 that the curves obtained under different excitation conditions present the same features. The experimental curves present the net area of the considered characteristic emissions, as explained above, without any normalization. Thus, there is no fitting parameter introduced to scale the experiment to the simulation. The fitted parameters are the thicknesses, roughnesses and densities of all the layers and interlayers. The composition of the PtSi interlayer is also varied, whereas the composition of the superficial tantalum oxide is fixed to the stoichiometric Ta_2O_5. The features of the XRR curve are well reproduced. Regarding GIXRF, it can be seen that the simulated curves reproduce well the shape and position of the experimental features well for Cr and Ta. There are some discrepancies regarding the intensities, which we ascribe to errors in the fundamental parameters (absorption coefficients, photoionization cross sections, …), to some experimental misalignment and also to some uncertainty in the parameters governing the geometric factor (see the “XRR and GIXRF simulations” sub-section). The results are summarised in Table 2, together with those obtained for the “Cr 5 nm” and “Cr 15 nm” samples.

In Figure 4(e) we give the variation of the density throughout the stack. It takes into account the roughness of the various layers. It is clear that the stack is far from presenting sharp interfaces but the three Ta, Cr and Pt layers are easily identified. Finally, Figure 4(f) presents the angular and depth distribution of the incident electric field within the stack for the 12 keV excitation. The guiding effect is observed by the concentration of the electric field in the Cr layer for an angle of 0.5°.

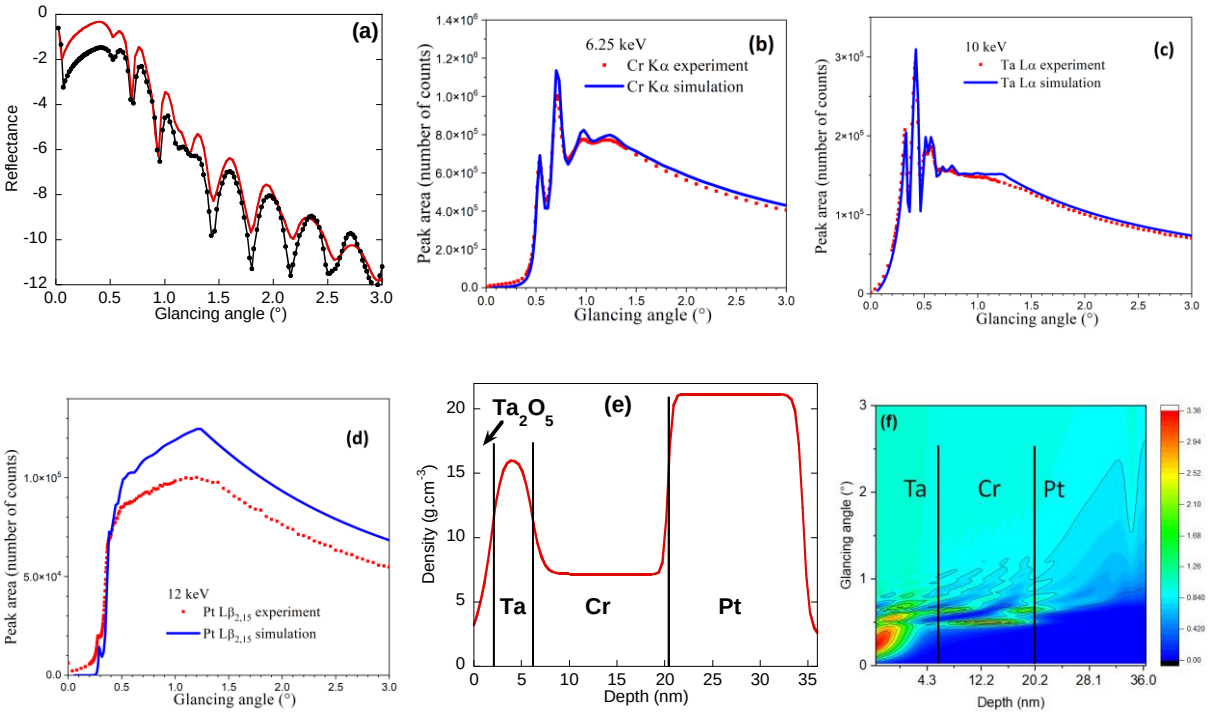

Figure 4: Simulations (lines) of the set of results (dots) of the sample “10 nm Cr” by a Ta_2O_5/Ta/Cr/Pt/PtSi/Si substrate model. (a) XRR curve (in log scale) at 6.25 keV; GIXRF curves (in linear scale) of (b) Cr at 6.25 keV, (c) Ta at 10 keV and (d) Pt at 12 keV; (e); variation of the density of the stack

as a function of the depth; (f) angular and depth distribution of the electric field within the stack for the 12 keV excitation. The colour scale gives the intensity of the electric field in an arbitrary unit.

Table 2: values of the fitted parameters used to describe the three studied samples by a Ta_2O_5/Ta/Cr/Pt/PtSi/Si substrate model. The number of atoms, deduced from the thicknesses and densities of the layers where these atoms are present, in both Ta and Ta_2O_5 layers for tantalum and in both Pt and PtSi layers for platinum, is indicated together with the deviation with respect of the values obtained from RBS. The composition of the PtSi layer in weight fraction is $Pt_{0.88}Si_{0.12}$. The thickness and roughness values are given with an absolute uncertainty of ±0.1 nm and the density with 10% relative uncertainty. Uncertainties are determined empirically by running many simulations.

Fitted parameters	"5 nm Cr"	"10 nm Cr"	"15 nm Cr"
thickness Ta_2O_5 (nm)	1.9	2.0	2.0
thickness Ta (nm)	3.9	4.1	4.1
thickness Cr (nm)	6.8	14.3	20.0
thickness Pt (nm)	13.8	13.8	13.8
thickness PtSi (nm)	0.7	0.2	0.6
roughness Ta_2O_5 (nm)	1.6	1.6	1.6
roughness Ta (nm)	1.0	1.0	1.0
roughness Cr (nm)	1.1	1.1	1.1
roughness Pt (nm)	0.5	0.5	0.5
roughness PtSi (nm)	0.6	0.7	0.6
roughness Si (nm)	0.7	0.7	0.7
density Ta_2O_5(g/cm^3)	5.9	5.9	5.9
density Ta (g/cm^3)	16.3	16.4	16.4
density Cr (g/cm^3)	7.15	7.15	7.15
density Pt (g/cm^3)	21.3	21.2	21.2
density PtSi (g/cm^3)	15.7	15.7	15.7
Ta (at/cm^2) Relative deviation from RBS	$2.43\ 10^{16}$ +16%	$2.57\ 10^{16}$ +0.6%	$2.57\ 10^{16}$ -4.5%
Cr (at/cm^2) Relative deviation from RBS	$5.63\ 10^{16}$ -3.9%	$11.84\ 10^{16}$ +2.7%	$16.56\ 10^{16}$ +5.5%
Pt (at/cm^2) Relative deviation from RBS	$9.38\ 10^{16}$ -10.7%	$9.12\ 10^{16}$ -9.7%	$9.12\ 10^{16}$ -11.8%

The results collected in Table 2 show that the three studied stacks can be described by the same structure formed of a succession of thin films:

- a superficial oxidized tantalum layer, about 2 nm thick;
- a tantalum metal layer, about 4 nm thick;
- a chromium layer, whose thickness varies linearly according to the number of deposited atoms, from 7 to 20 nm; the determined thicknesses are systematically one third larger than the aimed thicknesses owing probably to some calibration problem of the deposition system;
- a platinum layer, a little less than 14 nm thick;
- a very thin, less than 1 nm, platinum silicide layer formed following the interaction between the silicon atoms of the substrate and the deposited platinum atoms and having the PtSi

stoichiometry; owing to its small thickness, comparable to its roughness, this layer should be rather considered as a transition layer between the silicon substrate and the platinum layer.

The deduced densities of Cr, Ta and Pt layers are very close to those of the bulk materials. The density of the superficial Ta_2O_5 layer is much lower than the bulk, 8.2 g/cm^3, demonstrating that the choice of the stoichiometric composition is probably too simplistic. For each of the Ta_2O_5 and PtSi layers, the roughness is comparable to the thickness. This indicates that these are not well-defined layers but rather transition layers where density and composition are varying gradually.

Regarding the comparison of the numbers of Cr and Ta atoms determined by the XRR-GIXRF combination on one hand and RBS on the other hand, these numbers agree for the three samples, within the experimental uncertainty. The largest gap occurs for Ta in the “5 nm Cr” sample, for which the precision on the RBS determination is the lowest. Let us also note that if the XRR-GIXRF value is far from the RBS one, it is close to the XRR-GIXRF values determined for the two other samples. This is expected as during the deposition of the samples the same amount of tantalum was aimed for the series of samples. There is a problem with platinum whatever the sample. The number of atoms determined from XRR-GIXRF is systematically too low, about -11% which is larger than the associated uncertainties, with respect to the RBS determination. We also note that for Pt the overall agreement between the experimental and fitted GIXRF curves is poor, despite a good description of the shape of the curve, Fig. 4(d). This is valid for the three samples. We have verified, by suppressing or increasing slightly its thickness, that this discrepancy does not come from the thin platinum silicide layer introduced between the Si substrate and the thick Pt layer. So far, we do not have an explanation for this and suspect some possible diffusion of the platinum throughout the whole stack during the deposition process.

We do not indicate in Table 2 the number of oxygen atoms in the three samples. With the parameters of Table 2, this number would be for the three samples nearly 8.1 x 10^{15} O/cm^2, that is about half the ones given by the NRA measurement (see Table 1). However, we have verified that it would have been possible to introduce some oxidized layer in the stack, on top of the silicon substrate for example to consider the native oxide, without changing significantly the output of the fitting process. Thus, owing to the poor sensitivity of hard x-rays to the oxygen atoms, in our conditions the number of oxygen atoms is not relevant. A GIXRF experiment performed in the soft x-ray range, that is to say at photon energy much closer to the O 1s ionization threshold, would be much more sensitive to the oxygen atoms.

Conclusion

X-ray planar waveguides made of a few thin films can be used to probe the buried interfaces between solids at the nanoscale. In this framework, a series of Ta/Cr/Pt waveguides was studied by a combination of non-destructive and complementary methods: x-ray reflectivity and grazing incidence x-ray fluorescence. The measurements were performed in the hard x-ray range (photon energy higher than 5 keV) for incident, reflected and emitted radiations. The combined fit of the XRR and GIXRF data tightened constraints on the many parameters used to model the stacks and also showed that the thicknesses of the Ta and Cr layers are smaller than expected. The constraints on the parameters were further tightened by comparing the number of atoms as calculated from the thicknesses and densities of the layers to that measured by Rutherford backscattering spectrometry. This methodology

demonstrated that the Ta/Cr/Pt description is too simplistic: it was necessary to introduce some interlayers at the top and bottom of the stacks, but no interlayers between the Ta and Cr layers or between the Cr and Pt layers.

Acknowledgments

The authors are grateful to Pascal Mercère and Paulo Da Silva for assistance on the Metrology beamline and to the SOLEIL staff for smoothly running the facility.

References

[1] J. Zegenhagen and A. Kazimirov, *The X-Ray Standing Wave Technique: Principles and Applications*, Vol. 7 (World Scientific, 2013).

[2] Y. Tu, Y. Yuan, K. Le Guen, J.-M. André, J. Zhu, Z. Wang, F. Bridou, A. Giglia, and P. Jonnard, *X-Ray Fluorescence Induced by Standing Waves in the Grazing-Incidence and Grazing-Exit Modes: Study of the Mg–Co–Zr System*, J. Synchrotron Radiat. **22**, 1419 (2015).

[3] K. Le Guen et al., *Kossel Effect in Periodic Multilayers*, J. Nanosci. Nanotechnol. **19**, 593 (2019).

[4] V. Szwedowski-Rammert, J. Baumann, C. Schlesiger, U. Waldschläger, A. Gross, B. Kanngießer, and I. Mantouvalou, *Laboratory Based GIXRF and GEXRF Spectrometers for Multilayer Structure Investigations*, J. Anal. At. Spectrom. **34**, 922 (2019).

[5] X.-S. Lin, L.-L. Zhang, J.-H. Xu, Y. He, Y. Zheng, S. Yan, D.-X. Liang, and A.-G. Li, *Quantitative Calculation of a Confocal Synchrotron Radiation Micro-X-Ray Fluorescence Imaging Technique and Application on Individual Fluid Inclusion*, J. Anal. At. Spectrom. **36**, 2353 (2021).

[6] F. Förste, L. Bauer, K. Heimler, B. Hansel, C. Vogt, B. Kanngießer, and I. Mantouvalou, *Quantification Routines for Full 3D Elemental Distributions of Homogeneous and Layered Samples Obtained with Laboratory Confocal Micro XRF Spectrometers*, J. Anal. At. Spectrom. **37**, 1687 (2022).

[7] S. Torrengo, D. Eichert, Y. Mazel, M. Bernard, Y. Ménesguen, M. C. Lépy, and E. Nolot, *Quantitative Depth-Profile Analysis of Transition Metal Nitride Materials with Combined Grazing-Incidence X-Ray Fluorescence and X-Ray Reflectometry Analysis*, Spectrochim. Acta Part B At. Spectrosc. **171**, 105926 (2020).

[8] M. Czyzycki, M. Kokkoris, and A.-G. Karydas, *A Mathematical Model for Deep Ion Implantation Depth Profiling by Synchrotron Radiation Grazing-Incidence X-Ray Fluorescence Spectrometry*, J. Anal. At. Spectrom. **35**, 2964 (2020).

[9] F. C. Bocquet, G. Mercurio, M. Franke, G. van Straaten, S. Weiß, S. Soubatch, C. Kumpf, and F. S. Tautz, *Torricelli: A Software to Determine Atomic Spatial Distributions from Normal Incidence x-Ray Standing Wave Data*, Comput. Phys. Commun. **235**, 502 (2019).

[10] T. Ohta, Y. Kitajima, H. Kuroda, T. Takahashi, and S. Kikuta, *A Possible Use of the Soft X-Ray Standing Wave Method for Surface and Interface Structure Analysis*, Nucl. Instrum. Methods Phys. Res. Sect. Accel. Spectrometers Detect. Assoc. Equip. **246**, 760 (1986).

[11] Z. M. Spolnik, M. Claes, R. E. Van Grieken, P. K. de Bokx, and H. P. Urbach, *Quantification in Grazing-Emission X-Ray Fluorescence Spectrometry*, Spectrochim. Acta Part B At. Spectrosc. **54**, 1525 (1999).

[12] O. Karslıoğlu, M. Gehlmann, J. Müller, S. Nemšák, J. A. Sethian, A. Kaduwela, H. Bluhm, and C. Fadley, *An Efficient Algorithm for Automatic Structure Optimization in X-Ray Standing-Wave Experiments*, J. Electron Spectrosc. Relat. Phenom. **230**, 10 (2019).

[13] V. V. Lider, *X-Ray Divergent-Beam (Kossel) Technique: A Review*, Crystallogr. Rep. **56**, 169 (2011).

[14] J.-P. Zhang, C. Pendenque, K. Le Guen, R. Delaunay, I. Vickridge, D. Schmaus, Q.-G. Fu, and P. Jonnard, *Kossel Interferences of Proton-Induced X-Ray Emission Lines to Study Thin Film Waveguides*, Nucl. Instrum. Methods Phys. Res. Sect. B Beam Interact. Mater. At. **452**, 12 (2019).

[15] B. Caby et al., *Study of Annealing-Induced Interdiffusion in In2O3/Ag/In2O3 Structures by a Combined X-Ray Reflectivity and Grazing Incidence X-Ray Fluorescence Analysis*, Spectrochim. Acta Part B At. Spectrosc. **113**, 132 (2015).
[16] D. Ingerle, G. Pepponi, F. Meirer, P. Wobrauschek, and C. Streli, *JGIXA — A Software Package for the Calculation and Fitting of Grazing Incidence X-Ray Fluorescence and X-Ray Reflectivity Data for the Characterization of Nanometer-Layers and Ultra-Shallow-Implants*, Spectrochim. Acta Part B At. Spectrosc. **118**, 20 (2016).
[17] Y. Ménesguen et al., *CASTOR, a New Instrument for Combined XRR-GIXRF Analysis at SOLEIL*, X-Ray Spectrom. **46**, 303 (2017).
[18] W. Li, J. Zhu, X. Ma, H. Li, H. Wang, K. J. S. Sawhney, and Z. Wang, *Geometrical Factor Correction in Grazing Incident X-Ray Fluorescence Experiment*, Rev. Sci. Instrum. **83**, 053114 (2012).
[19] Y. Ménesguen and M.-C. Lépy, *COLEGRAM, a Flexible User-Friendly Software for Processing of Ionizing Radiation Spectra*, Nucl. Instrum. Methods Phys. Res. Sect. Accel. Spectrometers Detect. Assoc. Equip. **1003**, 165341 (2021).
[20] P. Jonnard and C. Bonnelle, *Cauchois and Sénémaud Tables of Wavelengths of X-Ray Emission Lines and Absorption Edges*, X-Ray Spectrom. **40**, 12 (2011).
[21] L. G. Parratt, *Surface Studies of Solids by Total Reflection of X-Rays*, Phys. Rev. **95**, 359 (1954).
[22] L. Névot and P. Croce, *Caractérisation Des Surfaces Par Réflexion Rasante de Rayons X. Application à l'étude Du Polissage de Quelques Verres Silicates*, Rev. Phys. Appl. **15**, 761 (1980).
[23] M. K. Tiwari and G. Das, *An Interactive Graphical User Interface (GUI) for the CATGIXRF Program – for Microstructural Evaluation of Thin Film and Impurity Doped Surfaces*, X-Ray Spectrom. **45**, 212 (2016).
[24] W. Pessoa et al., *Grazing Incident X-Ray Fluorescence Combined with X-Ray Reflectometry Metrology Protocol of Telluride-Based Films Using in-Lab and Synchrotron Instruments*, Spectrochim. Acta Part B At. Spectrosc. **149**, 143 (2018).
[25] A. Debski, R. Debski, and W. Gasior, *New Features of Entall Database: Comparison of Experimental and Model Formation Enthalpies/ Nowe Funkcje Bazy Danych Entall: Porównanie Doświadczalnych I Modelowych Entalpii Tworzenia*, Arch. Metall. Mater. **59**, 1337 (2014).